Image Anal Stereol 2020;39:33-46 doi:10.5566/ias.2245
*Original Research Paper*

# MODELING CRACK PATTERNS BY MODIFIED STIT TESSELLATIONS

ROBERTO LEÓN[1], WERNER NAGEL[✉,2], JOACHIM OHSER[3] AND STEVE ARSCOTT[4]

[1]Universidad Andrés Bello, Facultad de Ingeniería, Quillota 980, Viña del Mar, Chile; [2]University of Jena, Institute of Mathematics, 07737 Jena, Germany; [3]University of Applied Sciences, Department of Mathematics and Natural Sciences, Schöfferstr. 3, 64295 Darmstadt, Germany; [4]Institut d'Electronique, de Microélectronique et de Nanotechnologie (IEMN), CNRS, The University of Lille, Cité Scientifique, 59652 Villeneuve d'Ascq, France
e-mail: roberto.leon@unab.cl, werner.nagel@uni-jena.de, joachim.ohser@h-da.de, steve.arscott@univ-lille.fr
*(Received August 21, 2019; revised November 29, 2019; accepted December 2, 2019)*

ABSTRACT

Random planar tessellations are presented which are generated by subsequent division of their polygonal cells. The purpose is to develop parametric models for crack patterns appearing at length scales which can change by orders of magnitude in areas such as nanotechnology, materials science, soft matter, and geology. Using the STIT tessellation as a reference model and comparing with phenomena in real crack patterns, three modifications of STIT are suggested. For all these models a simulation tool, which also yields several statistics for the tessellation cells, is provided on the web. The software is freely available via a link given in the bibliography of this article. The present paper contains results of a simulation study indicating some essential features of the models. Finally, an example of a real fracture pattern is considered which is obtained using the deposition of a thin metallic film onto an elastomer material – the results of this are compared to the predictions of the model.

Keywords: fracture pattern, geometry-statistics, Monte Carlo simulation, random tessellation, STIT tessellation.

## INTRODUCTION

The main purpose of the paper is to develop a variety of mathematical models and modeling tools for the simulation of crack patterns. Our approach is based on ideas of stochastic geometry, in particular of random tessellations (random mosaics). We aim at providing parametric models which allow for a quantitative description of some classes of crack patterns.

The literature contains numerous examples of cracking and fracturing in fields ranging from geology and materials science to soft matter and nanotechnology. Often, these papers focus on the genesis and physics of an *individual* crack, *e.g.*, Thouless *et al.* (1987); Hutchinson and Suo (1991). However, there are also approaches to whole crack *patterns*, see *e.g.*, Xia and Hutchinson (2000); Iben and O'Brien (2006); Hafver *et al.* (2014); Boulogne *et al.* (2015); Seghir and Arscott (2015); Nandakishore and Goehring (2016); Kumar *et al.* (2017). Furthermore, also networks of roads are modeled as tessellations, see *e.g.*, Yu *et al.* (2014).

Being able to model and predict large surface cracking would be beneficial to those working in the above mentioned applied fields. This is the reason why we have developed the "Crack Pattern Simulator" (León, 2019).

We consider tessellations of the Euclidean plane $\mathbb{R}^2$ which are defined as a collection of convex polygons partitioning the plane. The polygons forming a tessellation are called cells.

The STIT tessellations – tessellations that are **ST**able under the operation **IT**eration of tessellations – were invented and first introduced in Nagel and Weiß (2005). This stochastic stability is an essential property which also allows for many theoretical results.

STIT tessellations belong to a class of random tessellations which are generated by consecutive division of their cells. There are two features of such a cell division process, as they were systematically introduced in Cowan (2010):

L The rule for the random *lifetime* of a cell, *i.e.*, the time between the birth of a cell by division of a mother cell, and the division of the cell.

D The rule for the random *division* of a cell at the end of its lifetime.

In these models it is assumed that the lifetime and the division of an extant cell only depend on the cell itself, and neither on the adjacent cells nor on the history of the division process.

The specification of these rules for STIT is described in the next section.

The realization of a planar STIT tessellation in Fig. 1 suggests that it can be a potential model for crack or fracture patterns as they arise in materials science, nanotechnology, geology, or drying soil patterns.

However, already tentative studies in Nagel *et al.* (2008) or Mosser and Matthäi (2014) indicated that for several patterns the STIT tessellations are not appropriate. This is not surprising because the STIT model emerged from purely mathematical ideas. Thus, an adaption of the cell division model to data of such fracture patterns is necessary. We have chosen a more "phenomenological approach", *i.e.*, we aim to model the geometric appearance, not focusing on the physics of crack formation.

In the present paper we suggest three modifications of the STIT model which are motivated by observations of fracture patterns. Briefly, the ideas are: when a cell is divided, the dividing line tends to be closer to the center of the cell than to the fringe of the cell. Therefore, we suggest the division rule D-GAUSS, which is introduced below.

Furthermore, the lifetime of a cell seems to depend rather on its area than on its perimeter, *i.e.*, the probability that a cell is divided at a certain moment is larger the larger its area is. This motivates the consideration of L-AREA, where the lifetime of a cell is exponentially distributed with its area as the parameter.

Firstly, we describe the planar STIT tessellation, and then we explain how to generate realizations by Monte Carlo simulation for a given directional distribution of the cell dividing lines.

In the second part of the paper we introduce the mentioned modifications of the STIT model, which are more flexible and thus potentially allow for a better adaption to actual fracture patterns. We present and explain the "Crack Pattern Simulation Tool" (León, 2019) for these models.

Furthermore, some quantitative results of a simulation study are given where we compare the models with respect to certain features.

In the last part of the paper we consider data from a real fracture pattern obtained using the deposition of a thin chromium/gold film onto an elastomer (polydimethylsiloxane, PDMS). A tensile stress in the layered material leads to film cracking. We check how good some statistical parameters can be fitted by the introduced models. A more detailed and thorough modeling will be the subject of forthcoming work.

# THE PLANAR STIT MODEL

Denoting by $\mathbb{R}^2$ the Euclidean plane and by $\mathscr{P}$ the set of all convex polygons, a subset $T \subset \mathscr{P}$ is called a tessellation if

(i) the polygons fill the plane, *i.e.*, $\bigcup_{z \in T} z = \mathbb{R}^2$,

(ii) the polygons do not overlap; more precisely, for all $z, z' \in T$, if $z \neq z'$, then $\operatorname{int} z \cap \operatorname{int} z' = \emptyset$, where $\operatorname{int} z$ denotes the topological interior of $z$,

(iii) $T$ is locally finite, *i.e.*, the set $\{z \in T : z \cap C \neq \emptyset\}$ is finite for all compact sets $C \subset \mathbb{R}^2$.

A random tessellation is a random variable with values in the set of all tessellations.

A construction of STIT tessellations in bounded windows in a Euclidean space of arbitrary dimension was described in all details in Nagel and Weiß (2005). A global construction, *i.e.*, in the whole space, was given in Mecke *et al.* (2008).

Here we give a description of the planar STIT tessellations in a convex polygon $W \subset \mathbb{R}^2$, referred to as the window. Let $\mathscr{H}$ denote the set of all lines in the plane. A line $H = H(\alpha, r) \in \mathscr{H}$ is parametrized by its normal direction $\alpha \in [0, \pi)$ and its signed distance $r$ from the origin, where the distance has a positive sign if the intersection of the line with its orthogonal subspace is in the upper half plane. For a line $H$ that does not contain the origin, denote by $H^+$ and $H^-$ the closed halfplanes generated by $H$, where $H^+$ contains the origin. Note that in our context the random lines contain the origin with probability zero. For a set $B \subset \mathbb{R}^2$ denote by $[B] = \{H \in \mathscr{H} : H \cap B \neq \emptyset\}$ the set of all lines intersecting $B$.

Up to a scaling factor, the distribution of a STIT tessellation is determined by the choice of a directional distribution $\varphi$, which is a probability distribution on the interval $[0, \pi)$. In Eq. 1 and Remark 1 it is explained how $\varphi$ determines the distribution of the lines dividing the cells. Throughout the paper, it is assumed that $\varphi$ is not concentrated on a single value. This guarantees that the constructed object is indeed a random tessellation (Schneider and Weil, 2008).

Based on $\varphi$, a translation invariant measure $\Theta$ on $\mathscr{H}$ is determined, up to a constant factor, by

$$\int_{\mathscr{H}} f(H)\Theta(\mathrm{d}H) = \int_{[0,\pi)} \int_{\mathbb{R}} f(H(\alpha, r))\, \mathrm{d}r\, \varphi(\mathrm{d}\alpha)$$

for any nonnegative measurable function $f : \mathscr{H} \to [0, \infty)$, see Section 4.4 of Schneider and Weil (2008). An interpretation of this formula and the application in the Monte Carlo simulation is given below.

For a convex polygon $z$ and a fixed direction $0 \leq \alpha < \pi$ denote by $h_0(z, \alpha) \leq h_1(z, \alpha)$ the two

values of the signed distances of the tangential lines to $z$ with normal direction $\alpha$. Formally, $h_0(z,\alpha) = \min\{x\cos\alpha + y\sin\alpha : (x,y) \in z\}$ and $h_1(z,\alpha) = \max\{x\cos\alpha + y\sin\alpha : (x,y) \in z\}$. Hence, a line $H(\alpha,r) \in [z]$, *i.e.*, $H(\alpha,r)$ divides $z$, if and only if $h_0(z,\alpha) < r < h_1(z,\alpha)$.

By $b(z,\alpha) = h_1(z,\alpha) - h_0(z,\alpha)$ we denote the value of the width (or breadth) function of $z$ in direction $\alpha$, *i.e.*, the distance of the two supporting (tangential) lines to $z$ which have the normal direction $\alpha$. The maximum width of $z$ is denoted by $b_{\max}(z) = \max_{0\le\alpha<\pi} b(z,\alpha)$, and the minimum width of $z$ is denoted by $b_{\min}(z) = \min_{0\le\alpha<\pi} b(z,\alpha)$.

By $\mathbf{1}\{\cdot\}$ we denote the indicator function which is 1 if the condition in $\{\cdot\}$ is satisfied, and 0 otherwise. For $0 < \alpha_0 \le \pi$ and a convex polygon $z$ we obtain

$$\Theta(\{H(\alpha,r) \in [z] : 0 < \alpha < \alpha_0\}) = \int_{[0,\pi)} \mathbf{1}\{0 < \alpha < \alpha_0\}\, b(z,\alpha)\, \varphi(\mathrm{d}\alpha)\,, \quad (1)$$

and in particular for $\alpha_0 = \pi$

$$\Theta([z]) = \int_{[0,\pi)} b(z,\alpha)\ \varphi(\mathrm{d}\alpha)\,. \quad (2)$$

Hence, $\Theta([z])$ can be understood as the $\varphi$-weighted mean width of $z$. If $\varphi$ is the uniform distribution on $[0,\pi)$ then $\Theta([z]) = P(z)/\pi$, where $P$ denotes the perimeter.

For a convex polygon $z$ we define a probability distribution $\Theta_{[z]}$ on the set $[z]$ of all lines which intersect $z$ by

$$\Theta_{[z]}(\cdot) = \Theta(\cdot \cap [z])/\Theta([z])\,.$$

**Remark 1** *Notice that according to Eq. 1 the directional distribution of a line which intersects a polygon $z$ is not $\varphi$ itself, but it is $\varphi$ endowed with the density $b(z,\alpha)/\Theta([z])$. This must be taken into account when a dividing line is generated in the Monte Carlo simulation of a STIT tessellation.*

A loose and informal description of the STIT tessellation process is:

L-STIT A cell $z$, that is born by the division of a larger cell, has a random lifetime which is exponentially distributed with parameter $\Theta([z])$.

D-STIT At the end of its lifetime, $z$ is divided by a random line $H$ with law $\Theta_{[z]}$, independent of the lifetime, and conditionally independent, given $z$, of all the dividing lines used before.

To give a formalized definition of the STIT tessellation process, let $\mathbb{N}$ denote set of positive integers and let $\underline{\tau} = (\tau_n : n \in \mathbb{N})$ be a sequence of independent and identically distributed (i.i.d.) random variables, exponentially distributed with parameter 1. The lifetime of a cell $z_i$ will be $\tau_i/\Theta([z_i])$, *i.e.*, exponentially distributed with parameter $\Theta([z_i])$.

Let $W \in \mathscr{P}$ be a convex polygon, referred to as a window. Now we define the process $(Y_{t,W} : t > 0)$ of STIT tessellations, restricted to the window $W$. The birth time of a cell $z$ is denoted by $\beta(z)$. This definition looks rather involved but its advantage is that it at once provides an algorithm for the STIT construction.

**Definition 1** The STIT tessellation process $(Y_{t,W} : t > 0)$ in $W$, driven by the measure $\Theta$ *is defined by*

*(a)* Initial setting.
*$Y_{t,W} = \{W\}$ for $0 < t < \tau_1/\Theta([W])$, $\beta(W) = 0$ and $z_1 = W$.*

*(b)* Recursion.
*For $t > 0$, let be $Y_{t,W} = \{z_{i_1},\dots,z_{i_n}\}$, i.e., $\beta(z_{i_k}) < t$ and $\beta(z_{i_k}) + \tau_{i_k}/\Theta([z_{i_k}]) \ge t$ for $k = 1,\dots,n$.*
*Define $i^* \in \{i_1,\dots,i_n\}$ as the index of the cell which is the next to be divided, such that*

$$\begin{aligned} t_{i^*} &= \beta(z_{i^*}) + \tau_{i^*}/\Theta([z_{i^*}]) \\ &= \min\left\{\beta(z_{i_k}) + \tau_{i_k}/\Theta([z_{i_k}]) : k = 1,\dots,n\right\}. \end{aligned}$$

*Then $Y_{t,W}$ remains constant until the jump at time $t_{i^*}$, when the process jumps, by division of the cell $z_{i^*}$ into the state*

$$Y_{t_{i^*},W} = (\{z_{i_1},\dots,z_{i_n}\} \setminus \{z_{i^*}\}) \cup \{z_{2n}, z_{2n+1}\}$$

*with $z_{2n} = z_{i^*} \cap H_{i^*}^+$, $z_{2n+1} = z_{i^*} \cap H_{i^*}^-$, where $H_{i^*}$ is a random line with law $\Theta_{[z_{i^*}]}$ and independent of $\underline{\tau}$ and conditionally independent, given $z_{i^*}$, of the $n-1$ dividing lines used before.*
*The birth time of the dividing line and of the new cells is $\beta(H_{i^*}) = \beta(z_{2n}) = \beta(z_{2n+1}) = t_{i^*}$.*

When $z_i$ is divided, the cell $z_i$ is replaced by its two daughter cells $z_i \cap H_i^+$ and $z_i \cap H_i^-$ with birth time $\beta(z_i \cap H_i^+) = \beta(z_i \cap H_i^-) = \beta(z_i) + \tau_i/\Theta([z_i])$. At any fixed time $t$ the tessellation $Y_{t,W}$ is a STIT tessellation, restricted to the window $W$.

A crucial feature of the construction is that the parameter of the exponentially distributed lifetime depends on the size of the cell, expressed by $\Theta([z])$, such that smaller cells have a longer expected lifetime than larger ones. In the particular case when

the measure $\Theta$ is isotropic, *i.e.*, $\varphi$ is the uniform distribution on $[0,\pi)$, the parameter of the exponential lifetime distribution of a cell $z$ is $\Theta([z]) = P(z)/\pi$, the perimeter of $z$ divided by $\pi$.

**Remark 2** *Even if this construction is performed in a fixed and bounded window $W$ it provides a distribution that is spatially consistent in the following sense. Let $W' \subset W$ be a convex polygon, $(Y_{t,W'} : t > 0)$ and $(Y_{t,W} : t > 0)$ the STIT tessellation processes generated in $W'$ and $W$, respectively. The symbol $\stackrel{D}{=}$ stands for the identity of distributions of random variables. Then for all $t \geq 0$ we have that*

$$Y_{t,W'} \stackrel{D}{=} \{z \cap W' : z \in Y_{t,W}, W' \cap \operatorname{int} z \neq \emptyset\} ,$$

*i.e., the restriction of $Y_{t,W}$ to $W'$ has the same distribution as $Y_{t,W'}$. This consistency property yields that, for any $t > 0$, there exists a spatially stationary (or homogeneous, which means the invariance of the distribution under translations of the Euclidean plane) random tessellation $Y_t$ of $\mathbb{R}^2$ such that the restriction of $Y_t$ to $W$ has the same distribution as $Y_{t,W}$ for all polygons $W \in \mathscr{P}$.*

The process $(Y_t : t > 0)$ has the following scaling property

$$t \cdot Y_t \stackrel{D}{=} Y_1 , \quad \text{for all } t > 0, \tag{3}$$

where $t \cdot Y_t = \{t \cdot z : z \in Y_t\}$ and $t \cdot z = \{tx : x \in z\}$. This space-time relation of the STIT tessellation process can be taken into account in the design of a simulation study.

## SIMULATION OF PLANAR STIT TESSELLATIONS

In León (2019) we provide a simulation tool which is described in the present section. The window $W$ is a square of side length $a$, which can be chosen in the range $a \in \mathbb{N}$, *i.e.*, a positive integer, *e.g.*, $a = 1$. Then one has to choose the time $t_{\text{STOP}} \in \mathbb{N}$, at which the construction stops, *e.g.*, $t_{\text{STOP}} = 50$. Regarding the scaling property Eq. 3 it would – theoretically – be sufficient to choose $t_{\text{STOP}} = 1$, but in order to obtain a reasonable number of cells in a simulation, the value of $t_{\text{STOP}}$ should be chosen in an appropriate relation to $a$.

While the choice of $a$ and $t_{\text{STOP}}$ is an issue of scaling, the selection of a directional distribution $\varphi$ for the cell dividing lines is an essential ingredient of a STIT tessellation model. By $\delta_\alpha$ we denote the Dirac measure, concentrated on a single value $0 \leq \alpha < \pi$, *i.e.*, $\delta_\alpha(B) = 1$ if $\alpha \in B$ and 0 otherwise, for a subset $B \subseteq [0,\pi)$. In the simulation tool one can choose one of the following directional distributions.

**List of directional distributions available in the simulation program**

ISO: The *isotropic distribution*, *i.e.*, $\varphi$ is the uniform distribution on the interval $[0,\pi)$.

DISCR: A *discrete distribution* with finitely many directions, *i.e.*, $\varphi = \sum_{i=1}^k p_i \delta_{\alpha_i}$, $2 \leq k$, with $0 \leq \alpha_i < \pi$ and probabilities $0 < p_i < 1$, $\sum_{i=1}^k p_i = 1$. In the generated tessellation solely segments with normal directions $\alpha_1, \ldots, \alpha_k$ appear. Once the number $k$ of directions is chosen, $2 \leq k \leq 32$ in León (2019), one has to insert the values $\alpha_i$ as the radian divided by $\pi$, *e.g.*, the input 0.5 means the angle $0.5\,\pi = 90°$. And for each $\alpha_i$ its probability $p_i$ has to be inserted.

DDISCR: A *disturbed discrete distribution*, *i.e.*, $\varphi = \left(\sum_{i=1}^k p_i \delta_{\alpha_i}\right) * \psi$, where $\psi$ is the elliptic distribution with parameter $b_{\text{ellip}}$, see ELLIP below. The $*$ denotes the convolution of measures. This means that a random 'disturbance' with an elliptic distribution is added to a direction, which is chosen from a discrete distribution DISCR.

RECT: The discrete distribution with horizontal and vertical directions only, and both with the same probability, *i.e.*, $\varphi = 0.5\,\delta_0 + 0.5\,\delta_{\pi/2}$, which is a particular case of DISCR. The tessellation consists of random rectangles.

DRECT: The discrete distribution RECT which is disturbed by the elliptic distribution ELLIP with parameter $b_{\text{ellip}} < 1$. This is a particular case of DDISCR.

ELLIP: An *elliptic distribution*. Consider an ellipse with horizontal half axis of length 1 and vertical half axis of length $b_{\text{ellip}} < 1$. Then the cumulative distribution function of $\varphi$ is defined as

$$F_\varphi(\alpha) = \frac{\text{area of ellipse sector } [0,\alpha]}{\text{half area of the ellipse}} , \quad 0 \leq \alpha < \pi.$$

Notice that for the value $b_{\text{ellip}} = 1$ we obtain the isotropic distribution ISO.

An elliptic distribution can be applied to model a compressed pattern as it appears in geological crack structures or rolled material, *cf.* Stoyan *et al.* (1980) and an analogon in 3 dimensions in Ohser and Schladitz (2009), p. 252.

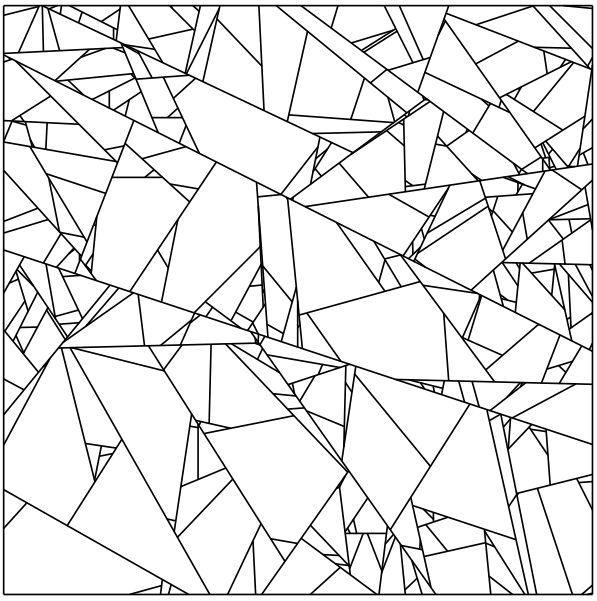

(a) ISO, $\mathrm{CV}(A) = 1.91$.

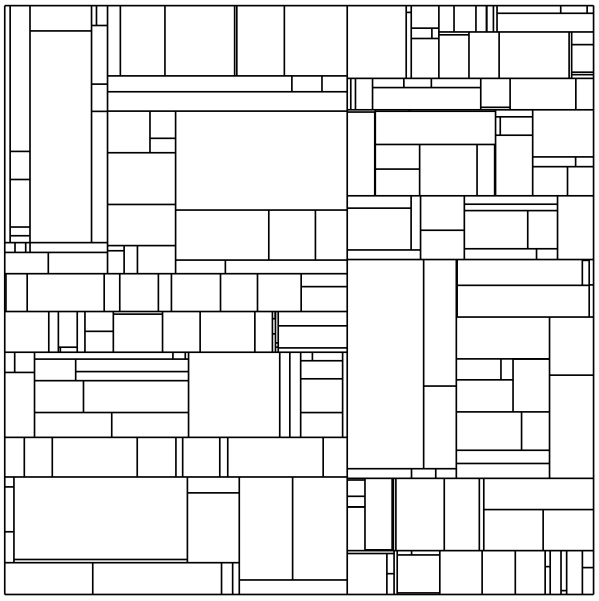

(b) RECT, $p_1 = p_2 = 0.5$, $\mathrm{CV}(A) = 1.67$.

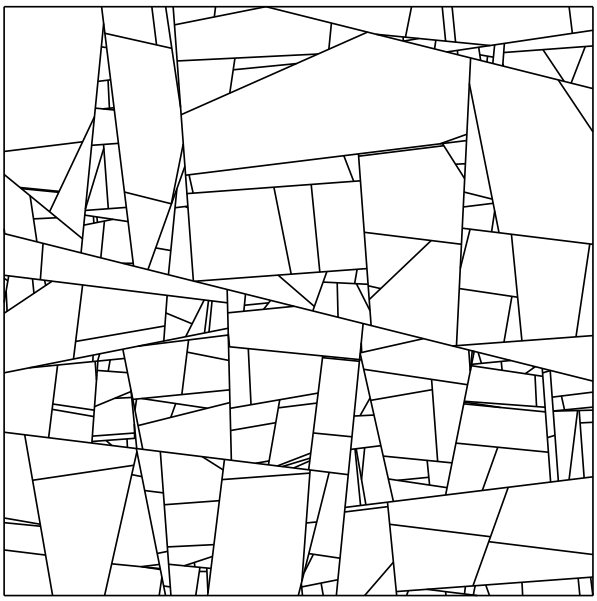

(c) DRECT, $p_1 = p_2 = 0.5$, $b_{\mathrm{ellip}} = 0.1$, $\mathrm{CV}(A) = 2.28$.

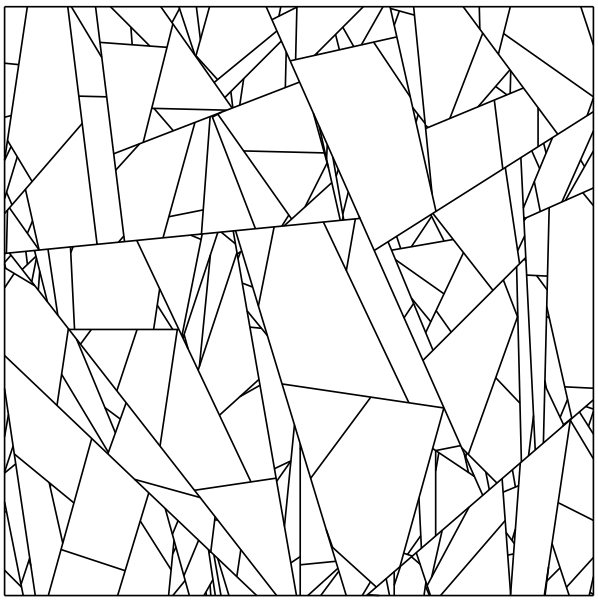

(d) ELLIP, $b_{\mathrm{ellip}} = 0.2$, $\mathrm{CV}(A) = 1.8$.

Fig. 1: Simulations of STIT tessellations with different directional distributions

Fig. 1 shows some examples of simulations of STIT tessellations for different directional distributions.

The algorithm for the Monte Carlo simulation of STIT tessellations follows Definition 1. The integral in Eq. 2, which is needed to determine the lifetime of an extant cell $z$, is discretized and replaced by a sum using 128 equidistant angles in $[0,\pi)$. This discretization proved to be sufficiently good for the directional distributions considered. Regarding Remark 1, the simulation of the direction of the line dividing a cell $z$ requires special attention, because it is not correct to generate the direction of the dividing line directly from $\varphi$. In León (2019) we apply a rejection method: For a given cell $z$, generate a direction $\alpha$ according to $\varphi$ and a random number $d$ which is uniformly distributed in the interval $[h_0(z,\alpha), h_0(z,\alpha) + b_{\max}(z)]$. The simulated line $H(\alpha,d)$ is *accepted* as a dividing line, if $d < h_1(z,\alpha)$, otherwise it is *rejected*. Recall that $h_0(z,\alpha) < h_1(z,\alpha)$ are the two signed distances of the tangential lines to $z$ with normal direction $\alpha$. If for a cell $z$ the dividing line is accepted, its random (signed) distance $d$ from the origin is *uniformly* distributed in the interval $[h_0(z,\alpha), h_1(z,\alpha)]$, *i.e.*, in the set of

those positions where the line intersects $z$. Thus, the direction of the accepted dividing line is correctly simulated according to Eq. 1.

## MODIFICATIONS OF THE STIT TESSELLATION

In order to extend the variety of models for crack tessellations, let us reconsider the items L and D given in the Introduction and modify the rules.

L-AREA The lifetime of a cell $z$ is exponentially distributed with parameter $A(z)$, where $A$ denotes the area.

D-GAUSS The simulation by the rejection method of the random direction of the cell dividing line is the same as in the STIT model. But then, for a cell $z$ and an accepted direction $\alpha$, the signed distance $d$ from the origin is not uniformly distributed in the interval $[h_0(z,\alpha), h_1(z,\alpha)]$, but according to a truncated (to the interval $[h_0(z,\alpha), h_1(z,\alpha)]$) Gaussian distribution with standard deviation $\sigma \cdot b(z,\alpha) = \sigma\,(h_1(z,\alpha) - h_0(z,\alpha))$ and mean $0.5(h_0(z,\alpha) + h_1(z,\alpha))$. Thus, $\sigma > 0$ is an additional parameter in this model. In the simulation tool one can choose it in the range $0 < \sigma < 1$. The smaller the value of $\sigma$ is chosen, the more concentrated to the center of the interval $[h_0(z,\alpha), h_1(z,\alpha)]$ is the random value of $d$.

Combining these rules, we focus on the following four types of models: (L-STIT, D-STIT), (L-STIT, D-GAUSS), (L-AREA, D-STIT), (L-AREA, D-GAUSS). In all of them, first choose a directional distribution $\varphi$. In the simulation tool León (2019) all the distributions ISO, DISCR, DDISCR and ELLIP listed above, can be combined with any of the four models.

**Remark 3** *Notice that essential properties of the STIT tessellation process, such as the spatial consistency and the scaling property are lost in the modified models. Therefore, the theoretical results proved for the STIT model cannot be applied. Up to a few exceptions, only simulation studies can be performed to investigate properties of these models.*

As the modifications of STIT lose the spatial consistency property, we cannot avoid edge effects, also in the generation of the tessellations. In order to attenuate the dependence on the chosen window $W$ in the models with D-GAUSS, we start the simulation with a simulation of a STIT tessellation process until a time $t_{\text{STOP}} \in \mathbb{N}$, and then, putting the clocks back to 0, the simulation of the modified model is launched until time $t_{\text{GAUSS}} \in \mathbb{N}$, but only in those cells of the generated STIT tessellation which do not intersect the boundary of the window $W$. Fig. 2 shows cut-outs of the simulations where the boundary cells are not seen, in order to provide a better impression of the models. The boundary cells are also not taken into account in the following statistical analysis.

Notice that until time $t_{\text{STOP}}$, the simulation yields an initial tessellation which is not the intended one – the result depending on the relation between $t_{\text{STOP}}$ and $t_{\text{GAUSS}}$. In order to see the effect of D-GAUSS, the value of $t_{\text{GAUSS}}$ should be large compared to $t_{\text{STOP}}$. In the example below with real data, we obtain good results with $t_{\text{STOP}} = 500$ and $t_{\text{GAUSS}} = 2000$. In our simulation studies, we have chosen $t_{\text{STOP}} = 32$, $t_{\text{GAUSS}} = 256$ and $t_{\text{STOP}} = 1024$, and $t_{\text{GAUSS}} = 2048$ respectively. Further examples are given in Fig. 2. When fitting a model to data, $t_{\text{STOP}}$ and $t_{\text{GAUSS}}$ can also be taken into account as additional parameters of the model.

## STATISTICS OF THE CELLS

The simulation tool León (2019) provides images of the simulated tessellations and thus a visual impression of the models. Furthermore, some quantitative features of the obtained tessellations are determined and presented. For the cells $z$ which do not intersect the boundary of the window $W$, we consider the area $A(z)$, the maximal width $b_{\max}(z)$, the minimal width $b_{\min}(z)$, the aspect ratio $ASR(z) = b_{\min}(z)/b_{\max}(z)$ and the isoperimetric quotient $RD(z) = 4\pi A(z)/P^2(z)$, where $P$ is the perimeter. In the literature the isoperimetric quotient is also referred to as roundness or sphericity. Notice that $ASR$ and $RD$ are invariant with respect to scaling.

For a given obtained tessellation, the mean value (MEAN), the mean squared error (MSE), the standard deviation (SD) and the coefficient of variation (CV) are shown.

The estimation of a cell statistic based on an obtained tessellation in a bounded window is biased. This is caused by edge effects. As the modifications of STIT are not spatially consistent, the edge effects cannot be treated exactly – even for those cells which are completely contained inside the window. Therefore, we cannot remove the bias, only reduce it. To do this, we apply an edge correction, inspired

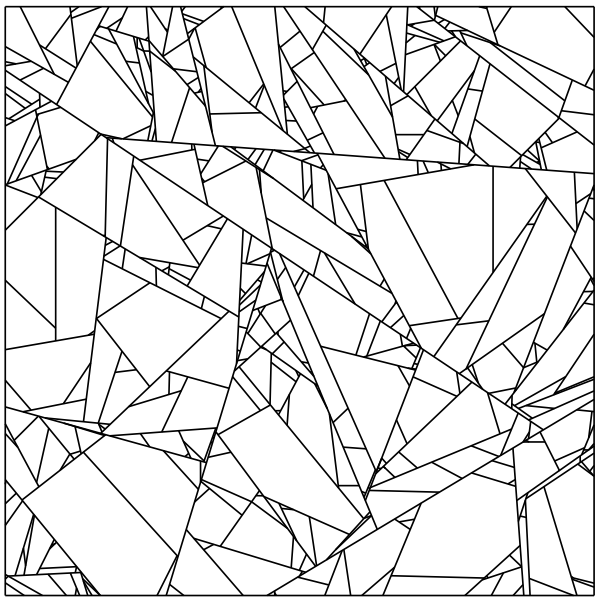

(a) (L-STIT, D-STIT), $t_{\text{STOP}} = 40$, $\text{CV}(A) = 1.95$

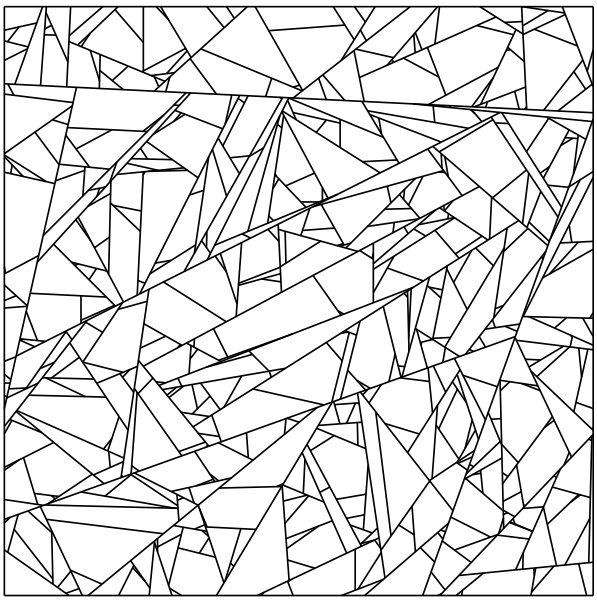

(b) (L-AREA, D-STIT), $t_{\text{STOP}} = 512$, $\text{CV}(A) = 1.26$

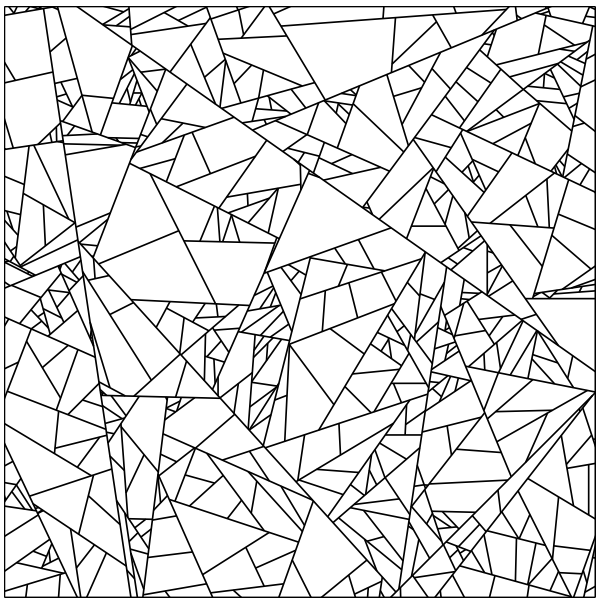

(c) (L-STIT, D-GAUSS), $\sigma = 0.01$, $t_{\text{STOP}} = 20$, $t_{\text{GAUSS}} = 35$, $\text{CV}(A) = 1.34$

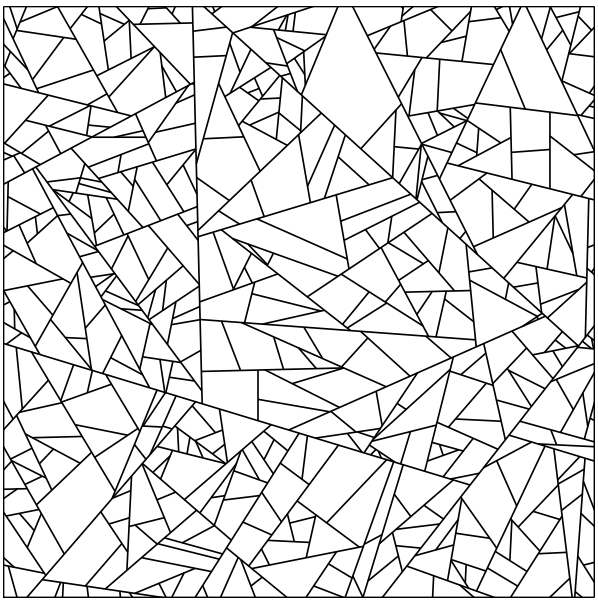

(d) (L-AREA, D-GAUSS), $\sigma = 0.01$, $t_{\text{STOP}} = 30$, $t_{\text{GAUSS}} = 450$, $\text{CV}(A) = 0.82$

Fig. 2: Simulations of isotropic tessellations with different lifetime distributions L and division rules D. In all the realizations are about 500 cells.

by the Miles-Lantuejoul method (Serra, 1982; Chiu *et al.*, 2013). Any cell which does not intersect the boundary of the window is given a weight, which is proportional to the reciprocal of the probability that this cell is completely contained in the window. This compensates for the different chances of the cells to appear completely inside the window. In a square window of side length $a$ and parallel to the horizontal and vertical axes, the weight of a cell $z \subset W$ is

$$w(z) = \frac{1}{(a - b(z,0))(a - b(z,\pi/2))} \, .$$

The formula to calculate the mean area of the cells in a given simulation is

$$\text{MEAN}(A) = \frac{1}{\sum_{z \subset W} w(z)} \sum_{z \subset W} w(z) A(z) \, ,$$

the mean squared error is

$$\mathrm{MSE}(A) = \frac{1}{\sum_{z\subset W} w(z)} \sum_{z\subset W} w(z)\,(A(z) - \mathrm{MEAN}(A))^2\,,$$

the estimated standard deviation is $\mathrm{SD}(A) = \sqrt{\mathrm{MSE}(A)}$, and the estimated coefficient of variation is $\mathrm{CV}(A) = \mathrm{SD}(A)/\mathrm{MEAN}(A)$.

For the other entities, the corresponding formulae are obtained by simply replacing the symbol $A$ by $P$, $RD$, $b_{\max}$, $b_{\min}$, $ASR$, respectively.

The isoperimetric quotient $RD$ and the aspect ratio $ASR$ are invariant with respect to scaling, and they provide information about the shapes of the cells. For all the entities the coefficient of variation CV is scale invariant and expresses the variability of these entities within a realization of the tessellation, *i.e.*, a small value of CV means that the structure is more 'homogeneous', *i.e.*, the differences between the individual cells are relatively small. The CV is a useful and efficient criterion for checking the goodness-of-fit of a model to a real structure.

Fig. 2 shows realizations of isotropic tessellations for the STIT model and for the three modifications. In (a) and (b) the simulation was performed in a window of size 1. For D-GAUSS the window size for the simulation was 2, and then the central part of size 1 was cut out and this is shown in (c) and (d). The times $t_{\mathrm{STOP}}$, and $t_{\mathrm{GAUSS}}$ are chosen such that in all cases there are about 500 cells. The very tiny cells are not visible in these panels. A comparison of the stopping times for L-STIT and L-AREA indicates that the division process is considerably slower when the lifetime distribution of the cells depends on the area.

## COMPARISON OF THE MODELS – A SIMULATION STUDY

Whereas there are numerous theoretical results for STIT tessellations, the modified models can (up to now) only be investigated by simulation studies. We have considered some examples in order to see how the modified models differ from STIT – and how they depend on the choice of their parameters.

Besides ISO and ELLIP, we focused on the directional distributions RECT and DRECT.

Some results of our simulation study are given in the Tables 1 and 2. The data are based on 100 repetitions of simulations with window side 1. The number of cells is indicated in order to show the sample sizes the estimated values are based on. Our focus is on the scale-independent CV-values, not on the number of cells. Clearly, the number of cells can be increased by increasing $t_{\mathrm{STOP}}$ or $t_{\mathrm{GAUSS}}$, respectively. But there is no theoretical basis to control the number of cells in the modified tessellation models.

In Figs. 3 and 4, for D-GAUSS the estimated values of $\mathrm{CV}(A)$ are plotted against $\sigma$, $0.1 \le \sigma \le 5$. For the elliptic directional distribution the parameter is $b_{\mathrm{ellip}} = 0.1$. The simulations for Fig. 3 are performed with $t_{\mathrm{STOP}} = 32$, $t_{\mathrm{GAUSS}} = 256$ and for Fig. 4 are performed with $t_{\mathrm{STOP}} = 1024$, $t_{\mathrm{GAUSS}} = 2048$. Each value is based on 50 repeated simulations in a window of size 1.

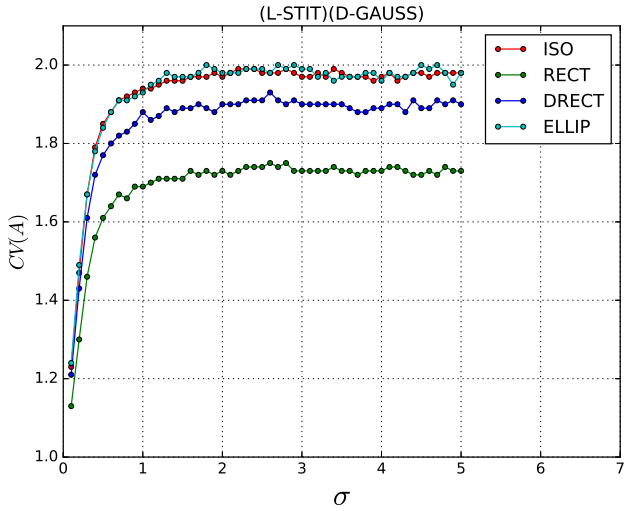


Fig. 3: The value of $\mathrm{CV}(A)$ as a function of $\sigma$ for (L-STIT, D-GAUSS).

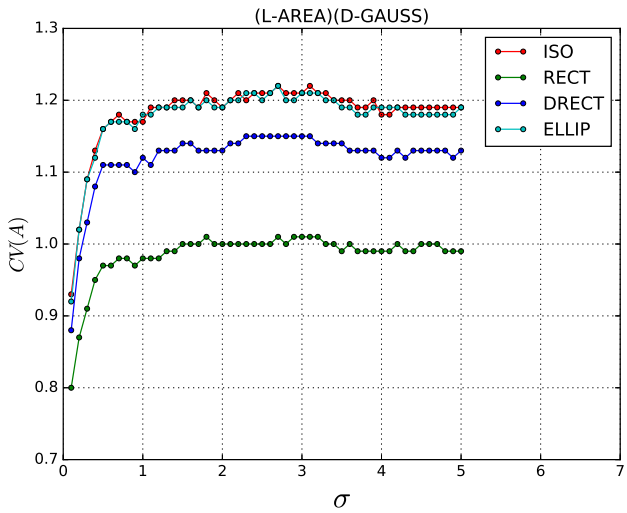


Fig. 4: The value of $\mathrm{CV}(A)$ as a function of $\sigma$ for (L-AREA, D-GAUSS).

We summarize our observations.

It can be seen in Tables 1 and 2 that $\mathrm{CV}(A)$ for (L-STIT, D-GAUSS) for $\sigma = 0.01$ is considerably smaller

Table 1: Values of CV for D-STIT with $t_{\text{STOP}} = 32$ for L-STIT and $t_{\text{STOP}} = 256$ for L-AREA. In the cases DRECT and ELLIP parameter $b_{\text{ellip}} = 0.05$.

| D-STIT | | L-STIT | | L-AREA | |
|---|---|---|---|---|---|
| | | CV | # cells | CV | # cells |
| ISO | Area | $1.84 \pm 0.27$ | $282 \pm 54$ | $1.17 \pm 0.09$ | $198 \pm 15$ |
| | Isoper. Quotient | $0.31 \pm 0.02$ | | $0.30 \pm 0.02$ | |
| | Max Width | $0.85 \pm 0.06$ | | $0.63 \pm 0.04$ | |
| | Min Width | $0.98 \pm 0.07$ | | $0.72 \pm 0.04$ | |
| | Aspect Ratio | $0.42 \pm 0.02$ | | $0.41 \pm 0.02$ | |
| RECT | Area | $1.63 \pm 0.21$ | $223 \pm 40$ | $0.98 \pm 0.07$ | $202 \pm 17$ |
| | Isoper. Quotient | $0.45 \pm 0.03$ | | $0.44 \pm 0.03$ | |
| | Max Width | $0.71 \pm 0.05$ | | $0.57 \pm 0.09$ | |
| | Min Width | $0.99 \pm 0.07$ | | $0.72 \pm 0.04$ | |
| | Aspect Ratio | $0.64 \pm 0.04$ | | $0.63 \pm 0.04$ | |
| DRECT | Area | $1.72 \pm 0.26$ | $227 \pm 45$ | $1.06 \pm 0.10$ | $202 \pm 16$ |
| | Isoper. Quotient | $0.45 \pm 0.03$ | | $0.45 \pm 0.02$ | |
| | Max Width | $0.75 \pm 0.06$ | | $0.59 \pm 0.06$ | |
| | Min Width | $0.99 \pm 0.08$ | | $0.72 \pm 0.04$ | |
| | Aspect Ratio | $0.56 \pm 0.03$ | | $0.56 \pm 0.03$ | |
| ELLIP | Area | $1.48 \pm 0.22$ | $77 \pm 18$ | $1.15 \pm 0.09$ | $167 \pm 15$ |
| | Isoper. Quotient | $0.57 \pm 0.05$ | | $0.57 \pm 0.04$ | |
| | Max Width | $0.79 \pm 0.07$ | | $0.68 \pm 0.05$ | |
| | Min Width | $0.92 \pm 0.10$ | | $0.74 \pm 0.05$ | |
| | Aspect Ratio | $0.70 \pm 0.08$ | | $0.71 \pm 0.05$ | |

Table 2: Values of CV for D-GAUSS with $\sigma = 0.01$ and $t_{\text{STOP}} = 32$, $t_{\text{GAUSS}} = 256$ for L-STIT and $t_{\text{STOP}} = 256$, $t_{\text{GAUSS}} = 512$ for L-AREA. In the cases DRECT and ELLIP parameter $b_{\text{ellip}} = 0.1$.

| D-GAUSS | | L-STIT | | L-AREA | |
|---|---|---|---|---|---|
| | | CV | # cells | CV | # cells |
| ISO | Area | $1.14 \pm 0.023$ | $19631 \pm 1293$ | $0.88 \pm 0.05$ | $383 \pm 23$ |
| | Isoper. Quotient | $0.20 \pm 0.002$ | | $0.26 \pm 0.01$ | |
| | Max Width | $0.52 \pm 0.005$ | | $0.49 \pm 0.03$ | |
| | Min Width | $0.54 \pm 0.005$ | | $0.52 \pm 0.02$ | |
| | Aspect Ratio | $0.31 \pm 0.002$ | | $0.37 \pm 0.02$ | |
| RECT | Area | $1.08 \pm 0.030$ | $12675 \pm 1142$ | $0.78 \pm 0.05$ | $406 \pm 28$ |
| | Isoper. Quotient | $0.21 \pm 0.006$ | | $0.35 \pm 0.02$ | |
| | Max Width | $0.51 \pm 0.008$ | | $0.54 \pm 0.06$ | |
| | Min Width | $0.57 \pm 0.009$ | | $0.55 \pm 0.03$ | |
| | Aspect Ratio | $0.37 \pm 0.006$ | | $0.51 \pm 0.03$ | |
| DRECT | Area | $1.13 \pm 0.025$ | $15792 \pm 1113$ | $0.85 \pm 0.05$ | $390 \pm 23$ |
| | Isoper. Quotient | $0.24 \pm 0.003$ | | $0.32 \pm 0.02$ | |
| | Max Width | $0.52 \pm 0.006$ | | $0.48 \pm 0.03$ | |
| | Min Width | $0.56 \pm 0.006$ | | $0.52 \pm 0.02$ | |
| | Aspect Ratio | $0.33 \pm 0.004$ | | $0.42 \pm 0.02$ | |
| ELLIP | Area | $1.14 \pm 0.039$ | $7521 \pm 1056$ | $0.88 \pm 0.06$ | $361 \pm 25$ |
| | Isoper. Quotient | $0.37 \pm 0.006$ | | $0.41 \pm 0.02$ | |
| | Max Width | $0.58 \pm 0.010$ | | $0.54 \pm 0.04$ | |
| | Min Width | $0.56 \pm 0.009$ | | $0.56 \pm 0.03$ | |
| | Aspect Ratio | $0.51 \pm 0.006$ | | $0.55 \pm 0.03$ | |

than for (L-STIT, D-STIT). This is not surprising, because for small values of $\sigma$ the lines tend to divide the cells more 'central', see also Fig. 2. The Fig. 3 and Fig. 4 illustrate the dependence on $\sigma$ of $\mathrm{CV}(A)$. The apparent limit for increasing $\sigma$ is plausible because the truncated Gauss distribution converges to the uniform distribution on the respective interval and thus the difference between D-GAUSS and D-STIT vanishes. It is remarkable, that even for very small $\sigma$ the $\mathrm{CV}(A)$ is never smaller than 1. We checked this also for values $\sigma = 10^{-4}$. This phenomenon is observed for all the considered directional distributions. Obviously, $\mathrm{CV}(A)$ also depends on the directional distribution, see Table 2. Notice, that in real crack patterns, as shown in the section below or in Nagel *et al.* (2008), $\mathrm{CV}(A)$ is clearly smaller than 1.

A reason for the apparently large lower bound for $\mathrm{CV}(A)$ is that the lifetime distribution L-STIT does not depend on the area of a cell $z$, but on $\Theta([z])$, which is for the directional distributions ISO and RECT proportional to the perimeter of $z$. This motivates an investigation of the (L-AREA, D-STIT) and (L-AREA, D-GAUSS) models. And indeed, the CV(A) is distinctly smaller than in the corresponding L-STIT models.

We remark, that for the (L-AREA, D-STIT) model with the directional distribution RECT we have a theoretic result that $\mathrm{CV}(A) = 1$ asymptotically, when the window side goes to infinity (a manuscript in preparation by Martínez and Nagel).

For (L-AREA, D-GAUSS), our simulations with $\sigma = 0.01$indicate, that for DRECT the $\mathrm{CV}(A)$ seems not considerably depend on the parameter $b_{\mathrm{ellip}}$, we observed CV(A)$\approx 0.7$ for all $0.001 \leq b_{\mathrm{ellip}} \leq 1$.

Qualitatively, $\mathrm{CV}(b_{\max})$ and $\mathrm{CV}(b_{\min})$ behave similar as $\mathrm{CV}(A)$, but quantitatively, the changes of the values are small.

In the cases which we considered, the CV of the isoperimetric quotient *RD* and of the aspect ratio *ASR* seems not to change significantly between L-STIT and L-AREA for the division rule D-STIT. But for the division rule D-GAUSS, the CV for L-AREA are larger than for L-STIT.

## AN EXAMPLE OF EXPERIMENTAL CRACKING

Sample preparation and microscopy: The experimental cracking shown in Fig. 5 was obtained by metallizing polydimethylsiloxane (PDMS).

The details of the fabrication can be found in a previous article (Seghir and Arscott, 2015) published by one of the authors. In the case here, the specific metallization was a chromium/gold (20/100 nm) bilayer film deposited using thermal evaporation. Prior to metallization, the PDMS had been treated with an appropriately-dosed oxygen plasma to create a thin brittle silica film on the surface of the PDMS – this brittle film enables the observed "mud-cracking" seen in Fig. 5. The cracking is due to the process-induced stress present in the thermally-evaporated chromium film – which is known to be high. The gold regions in the figure are the uniform chromium/gold layer, the black lines are the cracks in the metallization and the brittle silica surface layer. The large field image shown ($12 \times 8.7$ mm, $12\,425 \times 9\,021$ pixels of side length 0.96 µm) in the figure was produced using optical microscopy by stitching together 144 images using a digital microscope VHX-6000, Keyence, Japan. Fig. 6 shows zoom images of the cracking.

The result of image analysis is shown in Table 3. The area $A(z)$ of the cells is estimated by pixel counting, *i.e.*, $\hat{A}(z) = nc^2$, where $n$ is the pixel number and $c$ is the pixel size. The cells are convex, and hence the accuracy of $\hat{A}(z)$ can be estimated based on the Steiner formula (Schneider and Weil, 2008). Let $B_r$ denote the circle with radius $r$, centered in the origin, $\ominus$ and $\oplus$ the Minkowski subtraction and addition, respectively. From $z \ominus B_r \subseteq z \subseteq z \oplus B_r$ it follows for $r = c/12$ that

$$A(z) - \frac{c}{12}P(z) \lessapprox \hat{A}(z) \lessapprox A(z) + \frac{c}{12}P(z) + \frac{\pi c^2}{144}.$$

Hence, the relative deviation $\delta(\hat{A}) = (\hat{A}(z) - A(z))/A(z)$ from the true area $A(z)$ can be estimated by

$$\frac{cP(z)}{12A(z)} \lessapprox \delta(\hat{A}) \lessapprox \frac{12cP(z) + \pi c^2}{144A(z)}.$$

This formula shows the influence of the lateral resolution, expressed by $c$ on the error bounds. If, *e.g.*, $c = 1$ µm and $z$ is a square of the side length 20 µm, the above estimate yields $-1.667\,\% \lessapprox \delta(\hat{A}) \lessapprox 1.672\,\%$.

The estimation of the perimeter $P(z)$ is usually based on a discrete version of one of Crofton's intersection formulae (Ohser *et al.*, 1998), where the discretization is induced by the sampling of the continuous set $z$ on a square point lattice of spacing $c$. Let $\hat{P}(z)$ be an estimate of the perimeter and $\delta(\hat{P}) = \left(\hat{P}(z) - P(z)\right)/P(z)$. Then the Steiner formula and same arguments as for the area yield

$$-\frac{\pi c}{12P(z)} \lessapprox \delta(\hat{P}) \lessapprox \frac{\pi c}{12P(z)},$$

see also Ohser *et al.* (1998), where the accuracy of the perimeter estimation is treated in detail.

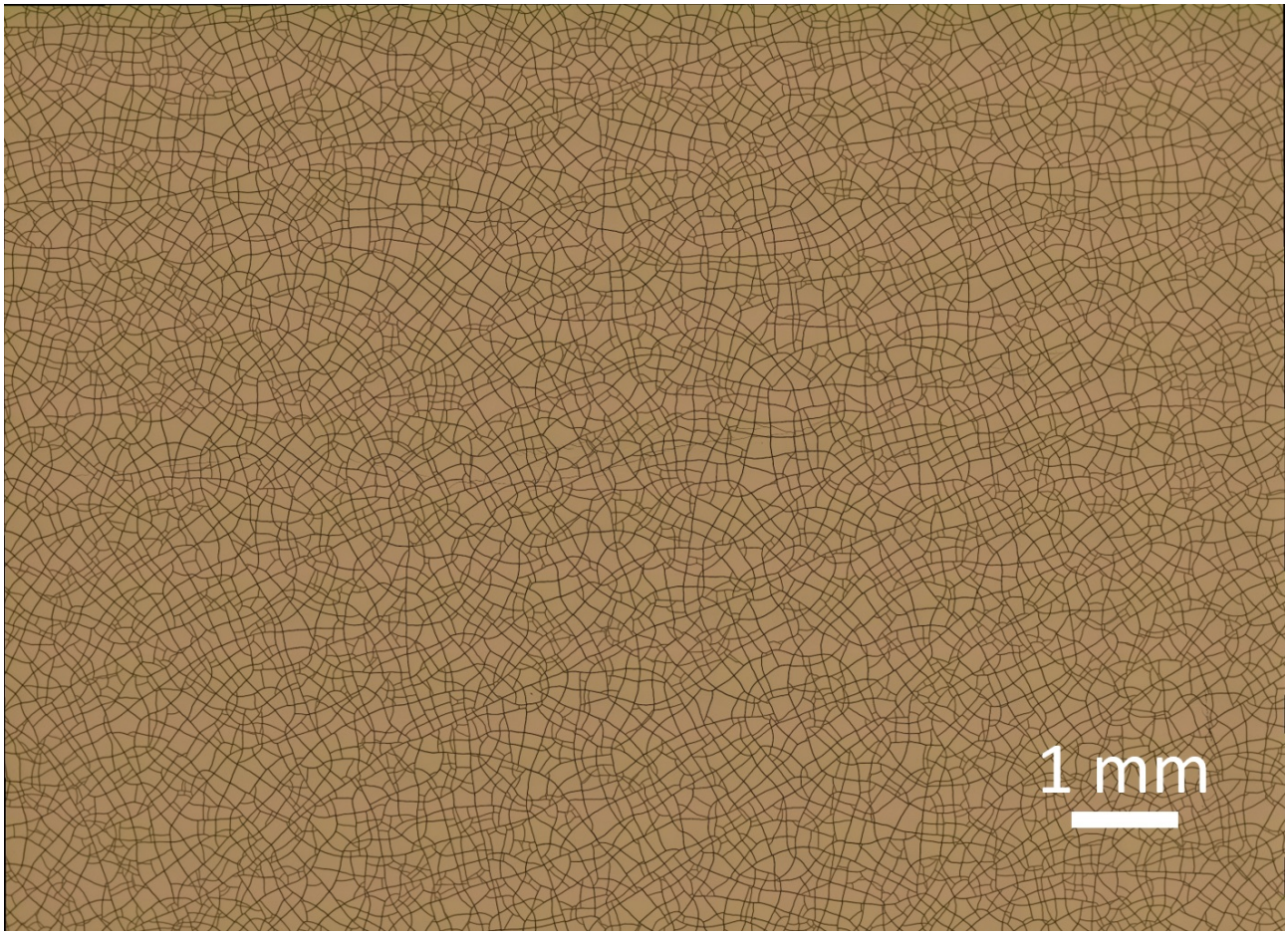


Fig. 5: Optical microscopy image of cracking of metallized (Cr/Au – 20/100 nm) PDMS. The metallization is indicated in gold, the cracks in black where the PDMS is visible. The metallization is a chromium/gold bilayer having a thickness of 20/100 nm. The image was taken using a digital optical microscopy VHX-6000, Keyence, Japan. The image ($12 \times 8.7$ mm, $12\,425 \times 9\,021$ pixels of side length 0.96 µm) is composed of 144 images stitched together.

The minimal and the maximal widths are estimated using the convex hull $C$ of the set of pixels belonging to $z$, where in our approach the convex hull was effectively determined using Graham's scan algorithm (Graham, 1972). The estimates are $\hat{b}_{\min}(z) = b_{\min}(C) + c$ and $\hat{b}_{\max}(z) = b_{\max}(C) + c$, respectively. Thus, the relative errors of these estimators should be between $-c/12$ and $c/12$.

As the isoperimetric quotient and the aspect ratio are ratios of random numbers, it is difficult to estimate their errors. However, it is expected that also for these ratios the errors decrease with decreasing pixel size $c$.

Nevertheless, for very small cells the relative error can be large. In our example, Fig. 5 consists of $12\,425 \times 9\,021$ pixels of side length 0.96 µm. Therefore, we believe that we have found a good balance of sufficiently high lateral resolution and sufficiently large sample size, as a basis for reasonable statistics.

Let us consider the sample of a crack pattern shown in Fig. 5 and check whether one of the presented models can approximately be fitted. At a first glance, one does not see preferred directions, and thus the overall directional distribution can be isotropic. But comparing the sample with the simulations for the directional distribution ISO, it becomes obvious that ISO will not be appropriate. In particular, in the sample the proportion of quadrangles is considerably higher than in the models with ISO. Therefore, we choose a disturbed discrete directional distribution DRECT with the parameter $0 < b_{\text{ellip}} < 1$.

The data in Table 3 and the results for $\mathrm{CV}(A)$ of our simulation study suggest to choose an (L-AREA, D-GAUSS) model and to look for appropriate parameter values.

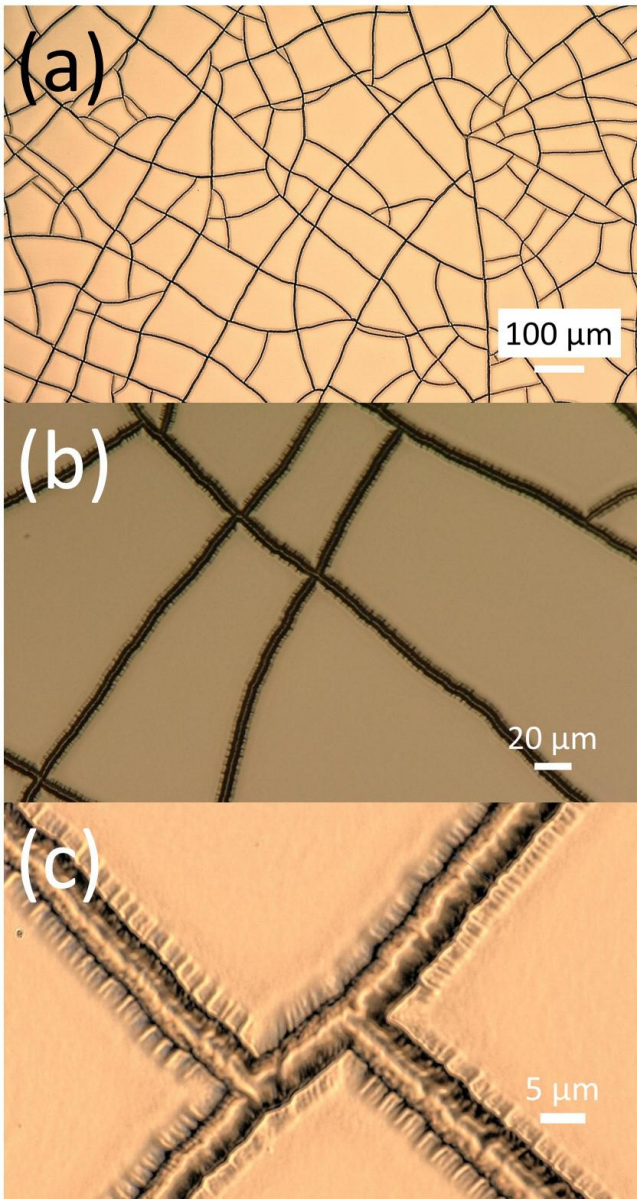


Fig. 6: Zoom images of the cracking taken using the optical microscope. (a) ×200 magnification/pixel size = 1.06 µm, (b) ×1000 magnification/pixel size = 0.2 µm, and (c) ×5000 magnification/pixel size = 0.044 µm. In (c) the crack width is $5.45 \pm 0.34$ µm.

As a first goodness-of-fit criterion we consider CV($A$), the coefficient of variation of the cell areas. It is a scale invariant statistic, and it is rather robust concerning digitization effects in image analysis.

As shown in Table 4, the choice $b_{\text{ellip}} = 0.1$, $\sigma = 0.1$, $t_{\text{STOP}} = 500$, $t_{\text{GAUSS}} = 2000$, window side $a = 1$, yields a good approximation for CV($A$). An obvious flaw is that the shape indicators MEAN($RD$) and MEAN($ASR$) are too small compared to the data in Table 3. Regarding an example of a tessellation as shown in Fig. 7, one can see that there appear numerous acute triangles which we do not observe in the sample in Fig. 5, and such triangles have small values of $RD$ and of $ASR$. It will be a subject of our future work to modify the model by suppressing small angles between the edges of the tessellations. Regarding the scale dependent entities, for the mean area and the mean perimeter, 1 unit of the simulation scheme corresponds to 894 µm and 750 µm, respectively. For Min Width the scaling factor is about 1000, and for Max Width it is about 700 which emphasizes the weak adaption of the model concerning the shape indicators.

Table 3: Statistical data for Fig. 5.

| | MEAN | SD | CV |
|---|---|---|---|
| Area (µm$^2$) | 403.515 | 319.725 | 0.794 |
| Perimeter (µm) | 75.075 | 31.185 | 0.415 |
| Isoper. Quotient | 0.787 | 0.109 | 0.138 |
| Min Width (µm) | 18.375 | 8.295 | 0.451 |
| Max Width (µm) | 28.56 | 11.445 | 0.401 |
| Aspect Ratio | 0.644 | 0.127 | 0.198 |

Table 4: Statistical data for simulated tessellations (50 replications) for (L-AREA, D-GAUSS), DRECT, $b_{\text{ellip}} = 0.1$, $\sigma = 0.1$, $t_{\text{STOP}} = 500$, $t_{\text{GAUSS}} = 2000$, window side $a = 1$.

| | MEAN | SD | CV |
|---|---|---|---|
| Area | 0.0005 | 0.0004 | 0.7896 |
| Perimeter | 0.0998 | 0.0423 | 0.4235 |
| Isoper. Quotient | 0.5759 | 0.1682 | 0.2921 |
| Min Width | 0.0168 | 0.0079 | 0.4688 |
| Max Width | 0.0411 | 0.0191 | 0.4648 |
| Aspect Ratio | 0.4385 | 0.1689 | 0.3853 |

## DISCUSSION

By starting with the pure mathematical STIT tessellation model, we have suggested some modifications to make the model more flexible – and introduced some parameters which can be varied and interpreted in order to adapt to data of real crack patterns. The simulation tool provided in León (2019) allows for experiments by a user who wants to check the applicability of the model.

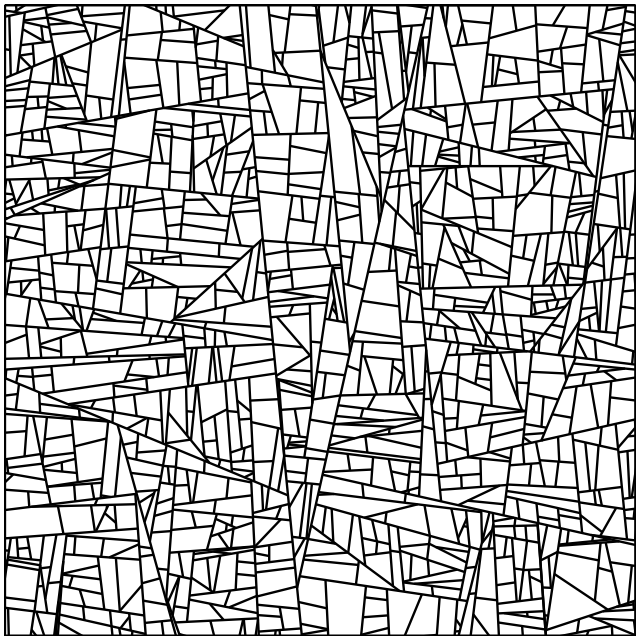

Fig. 7: Example of a simulated tessellation with (L-AREA, D-GAUSS), DRECT, $b_{\text{ellip}} = 0.1$, $\sigma = 0.1$, $t_{\text{STOP}} = 500$, $t_{\text{GAUSS}} = 2000$, window side $a = 1$.

The new models enable good results concerning the important statistical parameter $\text{CV}(A)$, the coefficient of variance of the cell areas. On the other hand, there are several obvious features of real crack patterns which are not yet understood, *e.g.*, in many crack patterns, a dividing line tends to meet at right angles with the boundary of the cell, rather than at small angles. This motivates future work aimed at feasible parametric models which allow for a reasonably good approximation of actual crack patterns.

## ACKNOWLEDGMENT

Werner Nagel was repeatedly supported by the Centro de Modelamiento Matemático (CMM) de la Universidad de Chile, Project Basal AFB170001 Conicyt.

The work of Steve Arscott was in part funded by the French 'RENATECH' network. The digital microscope was purchased within the French ANR funded project 'TIPTOP_1' (ANR-16-CE09-0029).

Matías Vargas from Facultad de Ingeniería de la Universidad Andrés Bello worked on the development of the simulation program web page.

The authors thank the referee and the editor for their helpful comments.

## REFERENCES

Boulogne F, Giorgiutti-Dauphiné F, Pauchard L (2015). Surface patterns in drying films of silica colloidal dispersions. Soft Matter 11:102–8.

Chiu SN, Stoyan D, Kendall WS, Mecke J (2013). Stochastic geometry and its applications, 3rd Ed. Chichester: John Wiley & Sons.

Cowan R (2010). New classes of random tessellations arising from iterative division of cells. Adv Appl Probab 42:26–47.

Graham RL (1972). An efficient algorithm for determining the convex hull of a finite planar set. Inform Process Lett 1:132–3.

Hafver A, Jettestuen E, Kobchenko M, Dysthe DK, Meakin P, Malthe-Sørenssen A (2014). Classification of fracture patterns by heterogeneity and topology. EPL Europhys Lett 105:56004.

Hutchinson J, Suo Z (1991). Mixed mode cracking in layered materials. Adv Appl Mech 29:63–191.

Iben HN, O'Brien JF (2006). Generating surface crack patterns. Graph Models 71:198–208.

Kumar A, Pujar R, Gupta N, Tarafdar S, G.U. K (2017). Stress modulation in desiccating crack networks for producing effective templates for patterning metal network based transparent conductors. Appl Phys Lett 111:013502.

León R (2019). Crack pattern simulation. http://crackpatternsimulation.informatica-unab-vm.cl/.

Mecke J, Nagel W, Weiß V (2008). A global construction of homogeneous random planar tessellations that are stable under iteration. Stochastics 80:51–67.

Mosser L, Matthäi S (2014). Tessellations stable under iteration. Evaluation of application as an improved stochastic discrete fracture modeling algorithm. In: Proc 2014 Int Discrete Fracture Network Eng Conf 163–76.

Nagel W, Mecke J, Ohser J, Weiß V (2008). A tessellation model for crack patterns on surfaces. Image Anal Stereol 27:73–8.

Nagel W, Weiß V (2005). Crack tessellations: characterization of stationary random tessellations stable with respect to iteration. Adv Appl Probab 37:859–83.

Nandakishore P, Goehring L (2016). Crack patterns over uneven substrates. Soft Matter 12:2253–63.

Ohser J, Schladitz K (2009). 3D images of materials structures – Processing and analysis. Weinheim, Berlin: Wiley VCH.

Ohser J, Steinbach B, Lang C (1998). Efficient texture analysis of binary images. J Microsc 192:20–8.

Schneider R, Weil W (2008). Stochastic and integral geometry. Berlin, Heidelberg: Springer.

Seghir R, Arscott S (2015). Controlled mud-crack patterning and self-organized cracking of polydimethylsiloxane elastomer surfaces. Sci Rep 5:14787–802.

Serra J (1982). Image analysis and mathematical morphology. London: Academic Press.

Stoyan D, Mecke J, Pohlmann S (1980). Formulas for stationary planar fibre processes. II. Partially oriented fibre systems. Math Operationsforsch Statist Ser Statist 11:281–6.

Thouless M, Evans A, Ashby M, Hutchinson J (1987). The edge cracking and spalling of brittle plates. Acta Metall Mater 35:1333–41.

Xia Z, Hutchinson J (2000). Crack patterns in thin films. J Mech Phys Solids 48:1107–31.

Yu X, Courtat T, Martins P, Decreusefond L, Kelif JM (2014). Crack STIT tessellations for city modeling and impact of terrain topology on wireless propagation. In: Proc 12th IEEE Int Symp Model Optim Mobile AdHoc Wireless Netw (WiOpt) 22-9.